Journal of Nuclear Materials 585 (2023) 154584

Contents lists available at ScienceDirect

Journal of Nuclear Materials

journal homepage: www.elsevier.com/locate/jnucmat

γ-photons and high-energy electrons produced by neutron irradiation in nuclear materials

Luca Reali [a,*], Mark R. Gilbert [a], Max Boleininger [a], Sergei L. Dudarev [a,b]

[a] CCFE, United Kingdom Atomic Energy Authority, Culham Science Centre, Oxfordshire OX14 3DB, UK
[b] Department of Physics and Thomas Young Centre, Imperial College London, South Kensington Campus, London SW7 2AZ, United Kingdom

ARTICLE INFO

Dataset link: https://doi.org/10.14468/hyde-5x49

Keywords:
Neutron-materials interaction
Nuclear gamma emission
High-energy electrons
Fusion reactor materials

ABSTRACT

Neutrons interacting with atomic nuclei in most of the materials included in the current fusion reactor designs—notably tungsten, ferritic and stainless steels, copper alloys—generate a γ-photon flux that is comparable in magnitude and energy with that of the neutrons, and which in turn generates an intense flux of high-energy electrons in the materials themselves. The occurrence of these γ- and electron fluxes has implications, among others, for the mobility of crystal defects in the materials, for the stability of the plasma, and for the internal heating of reactor components. While a highly spatially resolved numerical calculation of neutron, photon, and electron fluxes on the reactor scale is computationally unfeasible, it is possible to provide estimates based on solutions of Boltzmann's transport equation in a stationary and homogeneous material. Within their limits of validity, these estimates are robust and straightforward and they enable studying photon and electron generation in various materials, under different fission and fusion irradiation conditions and at various locations inside a reactor. We show that the irradiation environment provided by the IFMIF irradiation facility is similar to the expected fusion power plant conditions both in terms of the energy and intensity of photons and electrons generated by the neutrons in tungsten and steels.

1. Introduction

In the most notable thermonuclear fusion reaction,

$$^{2}_{1}\mathrm{D} + ^{3}_{1}\mathrm{T} \rightarrow ^{4}_{2}\mathrm{He}\ (3.5\ \mathrm{MeV}) + \mathrm{n}\ (14.1\ \mathrm{MeV}),$$

deuterium and tritium fuse to produce a helium atom and a neutron. The above deuterium-tritium (D-T) reaction has the largest fusion cross section and is therefore targeted in the current tokamak reactor designs involving magnetic plasma confinement [1]. The generation of electricity involves the conversion of the 14.1 MeV kinetic energy of the neutrons into heat, which occurs by means of several possible interactions between the neutrons and materials surrounding the plasma, primarily those that involve the generation of γ-photons. In fact, quoting H.T. Motz, "The usual fate of a neutron is to be absorbed by a nucleus with the consequent emission of gamma radiation" [2]. 14.1 MeV neutrons are effective at exciting nuclei deep in the bulk of materials, so much so that a source of such neutrons can be used for elemental characterisation, as reactions requiring a high neutron energy become accessible to detection [3].

There are different possible neutron-nucleus interactions, or reaction channels. The neutron can be elastically or inelastically scattered by a nucleus. The former is a billiard-ball collision; the latter is when the neutron is captured and the internal degrees of freedom of the nucleus are excited. The nucleus then undergoes de-excitation by emitting a neutron, which can be different from the captured one, and by the emission of γ-radiation [5]. These two reactions do not alter the nature of the nucleus. Other, more exotic, reactions can occur between a neutron and a nucleus, of which some lead to transmutation—a nuclide of one element transforming into a nucleus of another—with other pathways to transmutation being spontaneous decay of unstable isotopes via radioactive α and/or β decay [6]. These non-elastic reactions include (n, γ), (n, p), (n, α), (n, 2n), i.e. the capture of a neutron and subsequent emission of a γ-photon, a proton, an α-particle, or two neutrons, respectively. The likelihood associated with the various reaction channels depends both on the neutron energy and on the target nuclide. As an

* Corresponding author.
E-mail addresses: Luca.Reali@ukaea.uk (L. Reali), Mark.Gilbert@ukaea.uk (M.R. Gilbert), Max.Boleininger@ukaea.uk (M. Boleininger), Sergei.Dudarev@ukaea.uk (S.L. Dudarev).

https://doi.org/10.1016/j.jnucmat.2023.154584
Received 16 March 2023; Received in revised form 9 June 2023; Accepted 15 June 2023
Available online 20 June 2023

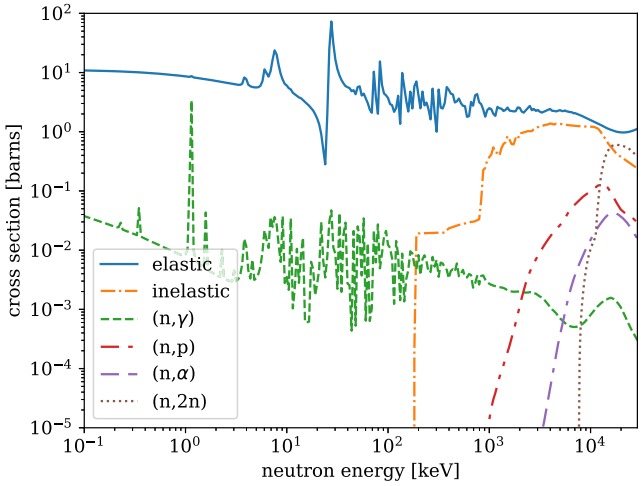

Fig. 1. Cross sections for several reaction channels in Fe: elastic, inelastic (where the incoming neutron is absorbed and another neutron is emitted), and four examples of non-elastic (where the neutron is absorbed causing a transmutation of the nuclide). Data were taken from Ref. [4].

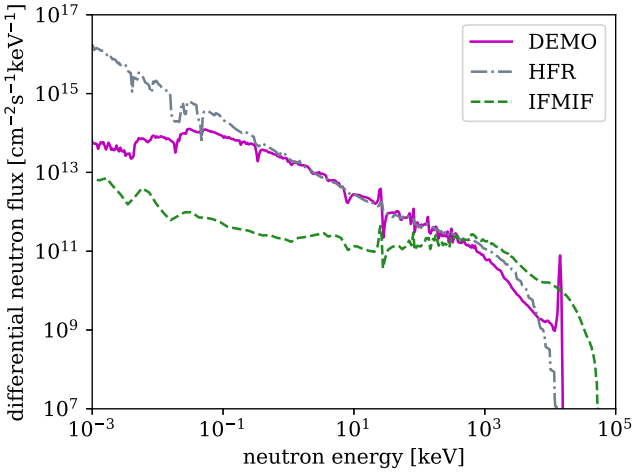

Fig. 2. Energy-resolved neutron spectrum in the fusion DEMO reactor, in the fission reactor HFR, and in the neutron irradiation facility IFMIF. The DEMO spectrum [17] corresponds to the flux simulated for the outboard equatorial first wall; the HFR is the C3 sample position [18], for example, shown in the reactor schematic (Fig. 1) in [19]; the IFMIF spectrum is for the D-Li source high flux test volume [20].

example, in Fig. 1 we plot the cross sections of the main nuclear reactions in Fe (evaluated as the abundance-weighted sum of the reactions on Fe's four stable isotopes, with atomic numbers 54, 56, 57, and 58). The cross sections were extracted from the TENDL-2021 nuclear data library [4].

Neutron-induced γ-photon generation occurs over a very wide time-scale window. Primary radiation is emitted by a nucleus during neutron-nucleus interactions over a time interval from 10^{-22} to 10^{-14} s. In most cases, multiple intermediate nuclear levels are traversed and multiple γ-photons are emitted; these short-lived levels have the lifetime of about 10^{-9} s. This is usually referred to as prompt γ-radiation [7]. For instance, 90% of the prompt γ-photons generated inside a concrete sample are emitted within 10 ns [8]. The de-excitation of an excited nucleus continues on a longer time-scale and produces delayed γ-radiation. For example, the half-life of the delayed γ-photons generated by ^{235}U is about 0.1 μs [9], but neutron capture reactions can also produce metastable nuclides that undergo radioactive decay with a much longer half-life of seconds or even longer [7].

Differently from nuclear fusion, a significant part of the energy released during fission reactions is carried away in the form of γ-photons. In fact, direct neutron collision-induced heating was found to be much smaller than γ-heating except in the case of low-Z elements [10–12]. In the core of a fast fission reactor, about 60% of the γ-heating comes from prompt γ-photons, 10% from inelastic scattering and 30% from delayed γ-photons [13].

The design of future fusion reactors must consider the effect of exposure of materials and components to the fusion irradiation environment. There is currently no fusion device operating at the foreseen commercial-reactor conditions that would deliver the expected damage rate in Fe of about 20 NRT-dpa/fpy (Norgett, Robinson, and Torrens displacement per atom per full power year) [14]. Hence, the behaviour of materials under these conditions has to be predicted on the basis of experiments performed either inside fission reactors or using designated neutron irradiation facilities. A notable example is the fusion-specific international fusion materials irradiation facility (IFMIF)-DONES currently being developed in Granada, Spain [15]; this facility evolved from the IFMIF/EVEDA project [16].

Since the cross sections that govern the neutron-nuclide interactions are highly energy-dependent, the starting point to predict the effects of a neutron-irradiation environment is the neutron energy spectrum. Fig. 2 compares the foreseen spectrum at the first wall location of a fusion DEMO reactor, the spectrum of the high flux reactor (HFR) located in Petten, the Netherlands, and the foreseen spectrum of IFMIF. The first is an example of a D-T fusion spectrum, where the 14.1 MeV peak is clearly visible, the second is an example of a fission scenario, the third represents one of the expected best materials characterisation facilities devoted to neutron irradiation. We refer an interested reader to Ref. [14] for a detailed comparison of the three scenarios. The next section outlines the steps required to calculate the photon and electron spectra generated by the neutron spectra such as those given in Fig. 2.

2. Photon and electron spectra from neutron irradiation

The Boltzmann transport equation (BTE) describes the local collisional equilibrium state of a system of particles, relevant examples of which are neutrons, photons and electrons. We summarise here the treatment developed in Ref. [12], where further details can be found. A central concept is the flux of particles, which can be neutrons, photons or electrons. We refer here to the scalar definition of the flux, denoted by $\phi(\mathbf{n}, \mathbf{x}, E)$, which is the number of particles crossing a unit area oriented perpendicular to $\mathbf{n}$, at position $\mathbf{x}$ in space and with energy E. Its generic units used in this study are $\mathrm{cm}^{-2}\,\mathrm{s}^{-1}\,\mathrm{keV}^{-1}$. Integration over energy $\int_0^\infty \phi(\mathbf{n}, \mathbf{x}, E)\mathrm{d}E$ gives the total flux for a specific position and direction.

We consider the linear formulation of the BTE, i.e. where scattering in the medium is included but not the interaction among the particles being transported. We moreover assume a dynamic equilibrium steady state, i.e. where partial derivatives with respect to time vanish. Under such conditions the BTE takes the form [21]

$$(\mathbf{n} \cdot \nabla)\,\phi(\mathbf{n}, \mathbf{x}, E) = I_{\mathrm{coll}}[\phi(\mathbf{n}, \mathbf{x}, E)] + Q(\mathbf{n}, \mathbf{x}, E), \tag{1}$$

where $\nabla = (\partial_x, \partial_y, \partial_z)$ is the gradient operator. The left-hand side of Eq. (1) has the physical meaning of the balance of particles entering and leaving the volume element at $\mathbf{x}$. The first term on the right-hand side, I_{coll}, is a functional that describes the collisions of the transported particles with the medium in which they propagate, whereas the second term Q represents the generation of new particles [21]. If the medium is homogeneous and the collision and generation terms are—on average—angularly isotropic, then the spatial gradient of the flux vanishes and we arrive at

$$I_{\mathrm{coll}}[\phi(\mathbf{n}, \mathbf{x}, E)] + Q(\mathbf{n}, \mathbf{x}, E) = 0. \tag{2}$$

The two terms in this equation have fundamentally different physical origins in the photon and in the electron cases. Let us consider the case of photons first.

BTE views the particles not individually, but rather as entities that are collectively found in an infinitesimal volume of phase space. Therefore, the collision must include a *negative* term to account for the interactions of the photons with the electrons in the material that cause them to leave the element of phase space in which they could be found, and a *positive* term to account for photons being scattered from higher energies and other directions of propagation into this phase space element. The collision term can be written as

$$I_{\text{coll}}[\phi(\mathbf{n},\mathbf{x},E)] = -n_0\sigma_{\text{tot}}(E)\phi_{\text{ph}}(\mathbf{n},\mathbf{x},E) + n_0\int \mathrm{d}E'\int \mathrm{d}\Omega'\frac{\mathrm{d}^2\sigma(\mathbf{n}',E'\to\mathbf{n},E)}{\mathrm{d}\Omega'\mathrm{d}E'}\phi_{\text{ph}}(\mathbf{n}',\mathbf{x},E'), \tag{3}$$

where n_0, not to be confused with the direction vector above, is the density of scattering centres. The second term in the right-hand side contains the differential cross section for a photon travelling in direction $\mathbf{n}'$ with energy E' to scatter into a state with direction $\mathbf{n}$ and energy E; the integration is performed over all the energies and all the elements of solid angle $\mathrm{d}\Omega$. At energies in the keV to MeV range, the three main interactions of photons with matter are photoelectric effect (PE), Compton scattering (CS), and pair production (PP) — the conversion of a photon into an electron-positron pair, energetically possible if the energy of the photon is at least twice the equivalent energy of the rest mass of the electron, or ~1.022 MeV. These three processes constitute the total cross section σ_{tot} in Eq. (3)

$$\sigma_{\text{tot}}(E) = \sigma_{\text{PE}}(E) + \sigma_{\text{CS}}(E) + \sigma_{\text{PP}}(E). \tag{4}$$

The numerical values for these cross sections are taken from a database [22]. However, since only during CS a photon emerges from the event, this is the only contribution to the second term on the right-hand side of Eq. (3). In a homogeneous neutron-irradiated material the generation term $Q(E)$ is isotropic and only a function of energy. It includes all the reactions between a neutron and a nucleus where photons are among the products of the reaction. This term will be described in detail in Section 3.1. Under the approximation that photon generation is only a function of energy, and since the CS process entering the integral term of Eq. (3) is also only a function of the incident photon energy, we arrive at a simplified transport expression for the photon flux

$$Q_{\text{ph}}(E) - n_0\sigma_{\text{tot}}(E)\phi_{\text{ph}}(E) + n_0\int \mathrm{d}E'\,K(E,E')\phi_{\text{ph}}(E') = 0, \tag{5}$$

where we have identified the kernel of the integral in Eq. (3) with

$$K(E,E') = \int \mathrm{d}\Omega'\frac{\mathrm{d}^2\sigma(\mathbf{n}',E'\to\mathbf{n},E)}{\mathrm{d}\Omega'\mathrm{d}E'}. \tag{6}$$

Eq. (5) can be solved iteratively. The leading term is found by neglecting CS from higher-energy photons as

$$\phi^{(0)}_{\text{ph}}(E) = \frac{Q_{\text{ph}}(E)}{n_0\sigma_{\text{tot}}(E)}. \tag{7}$$

The second term evaluates the flux contribution from CS of the photons making up the leading term, the third term does the same but considering the CS fraction of the second term, and so on, i.e.

$$\phi^{(i)}_{\text{ph}}(E) = \frac{1}{\sigma_{\text{tot}}(E)}\int \mathrm{d}E'\,K(E,E')\phi^{(i-1)}(E'). \tag{8}$$

We note that since kernel (6) contains only CS and $\sigma_{\text{tot}}(E)$ from Eq. (4) includes CS, PE and PP, each term in the series is smaller than the previous one. We then evaluate the flux by truncating the series to N terms

$$\phi_{\text{ph}}(E) = \phi^{(0)}_{\text{ph}}(E) + \sum_{i=1}^{N}\phi^{(i)}_{\text{ph}}(E). \tag{9}$$

We found that the flux was well-converged already at $N = 5$.

To find the expression for the kernel we use the Klein-Nishina cross section

$$\frac{\mathrm{d}\sigma}{\mathrm{d}\Omega} = \frac{r_{\text{c}}^2}{2}\left(\frac{E'}{E}\right)^2\left[\frac{E'}{E} + \frac{E}{E'} - \sin^2\theta\right], \tag{10}$$

which depends on the photon scattering angle θ and on the classical electron radius $r_{\text{c}} = 2.8179$ fm. Inserting the above expression into Eq. (6), we find

$$K(E,E') = \begin{cases} \frac{\pi r_{\text{c}}^2 mc^2}{E'^2}\left[\frac{E}{E'} + \frac{E'}{E} - 1 + \left(\frac{mc^2}{E'} - \frac{mc^2}{E} + 1\right)^2\right], & \frac{E'}{1+\frac{2E'}{mc^2}} < E < E' \\ 0, & \text{otherwise} \end{cases} \tag{11}$$

The source term $Q_{\text{ph}}(E)$ that is ultimately responsible for the flux generated in the bulk of the material is calculated using neutron transport codes by folding the cross section matrices of the γ-generating scattering events with the flux of neutrons. This operation is among the steps taken by the neutron transport codes such as OpenMC and MCNP, but it can also be performed by a dedicated computer program SPECTRA-PKA [23] by supplying, as recoil cross sections, the cross sections generated by the nuclear data processing code NJOY [24]. Typically, $Q_{\text{ph}}(E)$ is returned as an array of number of photons generated per unit time per atom having energy inside specified bin widths. This can be used to approximate the continuous source term function by dividing the discrete points by the corresponding bin width.

High-energy photons have mean free paths of the order of centimetres, and undergo a fairly small number of scatterings where they lose a large fraction of their energy before being absorbed (typically fewer than 5). On the other hand, high energy electrons have a much shorter mean free path and undergo many orders of magnitude more numerous scattering events where they typically lose only a small fraction of their energy [12,25–28]. Therefore, the scattering term for electrons with angularly isotropic distribution is usually written using the so-called continuous slowing down approximation [21,26,29]. Similarly to how neutron scattering provides the source term for γ-photons, the γ-photon scattering provides the source term $Q_{\text{el}}(E)$ for high-energy electrons, which is angularly isotropic for an angularly isotropic photon flux. If the electron flux is assumed to be only dependent on energy, the BTE (2) simplifies to

$$0 = \frac{\partial}{\partial E}[\bar{\varepsilon}(E)\phi_{\text{el}}(E)] + Q_{\text{el}}(E), \tag{12}$$

where $\bar{\varepsilon}(E)$ is the average rate of energy losses of an electron with energy E, whose values can be found in databases [30] and which is related to the range $R(E)$ of electrons defined as [21,29,31]

$$R(E) = \int_0^E \frac{\mathrm{d}E'}{\bar{\varepsilon}(E')}. \tag{13}$$

The solution of Eq. (12) can be written as

$$\phi_{\text{el}}(E) = \frac{1}{\bar{\varepsilon}(E)}\int_E^\infty \mathrm{d}E'\,Q_{\text{el}}(E'). \tag{14}$$

The source term in Eq. (14) is primarily given by the sum of three terms:

$$Q_{\text{el}}(E) = Q_{\text{PE}}(E) + Q_{\text{CS}}(E) + Q_{\text{PP}}(E). \tag{15}$$

Note that the three high-energy electron generation processes mirror the three photon scattering processes that were discussed above: the same scattering events that remove photons (PE, PP) or decrease their energy (CS) are transferring the photon energy to the electrons (cf. Eq. (4)).

Table 1
Photon and total heating in different materials.

Material	DEMO			HFR		
	total [W/g]	photon [W/g]	ratio	total [W/g]	photon [W/g]	ratio
W	2.73	2.65	97.1%	10.48	10.36	98.8%
Zr	1.06	0.835	78.8%	0.613	0.343	56.0%
Cu	1.79	1.28	71.5%	3.08	2.75	89.3%
Fe	1.68	1.19	70.8%	2.00	1.63	81.5%
Be	3.65	2.89×10^{-3}	0.08%	2.15	8.40×10^{-7}	0.00004%

During the photoelectric absorption, the energy of a photon is entirely transferred to an electron, provided that we neglect the binding energy that is about three or more orders of magnitude smaller than the photon energies of interest, hence

$$Q_{\mathrm{PE}}(E) = n_0 \sigma_{\mathrm{PE}}(E) \phi_{\mathrm{ph}}(E). \tag{16}$$

To treat the Compton scattering, we define an energy-differential cross section for the scattering of an electron with a given energy E by a photon with the initial energy E_{ph}. Since the scattered electron energy is the difference between the initial and final photon energy, starting from Eq. (11) we find that

$$\frac{\mathrm{d}\sigma}{\mathrm{d}E} = \begin{cases} \frac{\pi r_e^2 mc^2}{E_{\mathrm{ph}}^2}\left[\frac{E_{\mathrm{ph}}}{E_{\mathrm{ph}}-E} - \frac{E}{E_{\mathrm{ph}}} + \left(\frac{mc^2}{E_{\mathrm{ph}}} - \frac{mc^2}{E_{\mathrm{ph}}-E} + 1\right)^2\right], & 0 < E < \frac{2E_{\mathrm{ph}}^2}{2E_{\mathrm{ph}}+mc^2} \\ 0. & \text{otherwise} \end{cases} \tag{17}$$

The electron generation term associated with CS is

$$Q_{\mathrm{CS}}(E) = n_{\mathrm{el}} \int \mathrm{d}E_{\mathrm{ph}}\, \phi_{\mathrm{ph}}(E_{\mathrm{ph}}) \frac{\mathrm{d}\sigma}{\mathrm{d}E}(E_{\mathrm{ph}}, E). \tag{18}$$

The integrand in Eq. (18) gives the energy-differential frequency with which an electron acquires the energy E by CS in a energy-differential photon flux ϕ_{ph}. To find a volumetric generation term, we integrate over all the photon energies and multiply the result by the number of electrons per unit volume n_{el}. If the differential photon flux is available as a discrete array, i.e.

$$\phi_{\mathrm{ph}}(E_{\mathrm{ph}}) = \sum_{i=1}^{N} \Phi_{\mathrm{ph}}^{(i)} \delta(E_{\mathrm{ph}} - E_i), \tag{19}$$

where $\delta(E)$ is the Dirac delta function, we can simplify Eq. (18) to

$$Q_{\mathrm{CS}}(E) = n_{\mathrm{el}} \sum_{i=1}^{N} \Phi_{\mathrm{ph}}^{(i)} \frac{\mathrm{d}\sigma}{\mathrm{d}E}(E_i, E). \tag{20}$$

During PP, on the other hand, the photon energy is converted into an electron and a positron, each with their rest mass m and kinetic energy. The kinetic energy gained by the two particles can differ, but on average we assume equipartition by symmetry. The electron energy is then $E = \frac{1}{2}(E_{\mathrm{ph}} - 2mc^2)$ and the generation term is

$$Q_{\mathrm{PP}}(E) = n_0 \sigma_{\mathrm{PP}}(E_{\mathrm{ph}}) \phi_{\mathrm{ph}}(E_{\mathrm{ph}}). \tag{21}$$

The predictions of the formulae given in this section were compared, in Ref. [12], with the outcome of a fully numerical Monte-Carlo MCNP calculation, finding close agreement between the two approaches. The approximation in which electron binding effects are neglected also imply that the computed γ-spectra do not include the characteristic X-rays generated by the atomic core electrons. These X-rays, used in the energy-dispersion X-ray analysis (EDX) of materials [32], have relatively low integrated intensity even under strong electron beam exposure in a transmission electron microscope [33].

3. Results

3.1. Gamma heating and the spectrum of photon generation

First, we evaluate the nuclear heating in a pure material under neutron irradiation spectra representative of fusion and fission scenarios as given by the DEMO first wall and HFR reactor spectra, respectively, see Fig. 2. In Table 1, the total heat generation is shown alongside the fraction of heating ascribed to photon heating. The remaining balance represents heating caused by elastic nuclear collisions, or neutron heating. Table 1 shows the results for W, Zr, Cu, Fe and Be, expanding the results given in [12].

The heating considered here, i.e. the local energy deposition by neutrons, only considers prompt γ-photons. The contribution from delayed γ-photons, which is not included in standard Monte Carlo neutronics programmes, is expected to be about 30% of the total photon flux [11,13]. FISPACT-II [34] was used to calculate the energy deposition via the KERMA (Kinetic Energy Released per unit MAss) cross sections that are available from nuclear data libraries.

Second, we evaluate the photon generation term $Q_{\mathrm{ph}}(E)$ as it is required for computing the γ-photon and the high-energy electron spectra, see Eqs. (9) and (14), respectively. In order to demonstrate the influence of the target nucleus on this quantity, we computed $Q_{\mathrm{ph}}(E)$ using the DEMO first wall neutron spectrum for five different materials: three pure elements W, Zr, and Cu, an alloy denoted by Fe9.0Cr1.1W made of Fe with 9.0% Cr and 1.1% W by weight, and water. We refer to Fig. 3a for plots of the photon generation terms in these materials. Fe9.0Cr1.1W is very close in composition to the reduced activation ferritic martensitic Eurofer-97 alloy [35], as well as to alloy E911 for fission applications [36]. Appendix A contains a more detailed analysis where the photon generation in W and Fe9.0Cr1.1W is divided into the contributions generated by thermal, epithermal and fast neutrons. As it is shown there, thermal neutrons of this specific spectrum are responsible for less than 0.01% of the photons in both materials. Epithermal neutrons account for over 70% of photons generated in W whereas fast neutrons produce over 85% of photons in Fe9.0Cr1.1W. In W, the remaining ~30% of the photons that are produced by fast neutrons dominate the photon generation spectrum below about 100 keV and above about 10 MeV.

From the photon generation $Q_{\mathrm{ph}}(E)$ it is straightforward to find the cumulative photon generation $\mathcal{Q}_{\mathrm{ph}}(E)$. If $Q_{\mathrm{ph}}(E)$ is available as a continuous function then

$$\mathcal{Q}_{\mathrm{ph}}(E) = \int_{-\infty}^{E} Q_{\mathrm{ph}}(\mathcal{E})\mathrm{d}\mathcal{E}. \tag{22}$$

If it is a discrete array $Q_{\mathrm{ph}}^{(i)}$ like in our case, then

$$\mathcal{Q}_{\mathrm{ph}}^{(i)} = \sum_{j=1}^{i} Q_{\mathrm{ph}}^{(j)}. \tag{23}$$

The cumulative photon generation curves calculated from Fig. 3a are plotted in Fig. 3b. It should be noted that while $Q_{\mathrm{ph}}(E)$ is expressed in units of $\mathrm{s}^{-1}\,\mathrm{eV}^{-1}\,\mathrm{at}^{-1}$, $Q_{\mathrm{ph}}^{(i)}$ has units of $\mathrm{s}^{-1}\,\mathrm{at}^{-1}$. In practice, since the neutron processing codes operate with discrete arrays on an energy

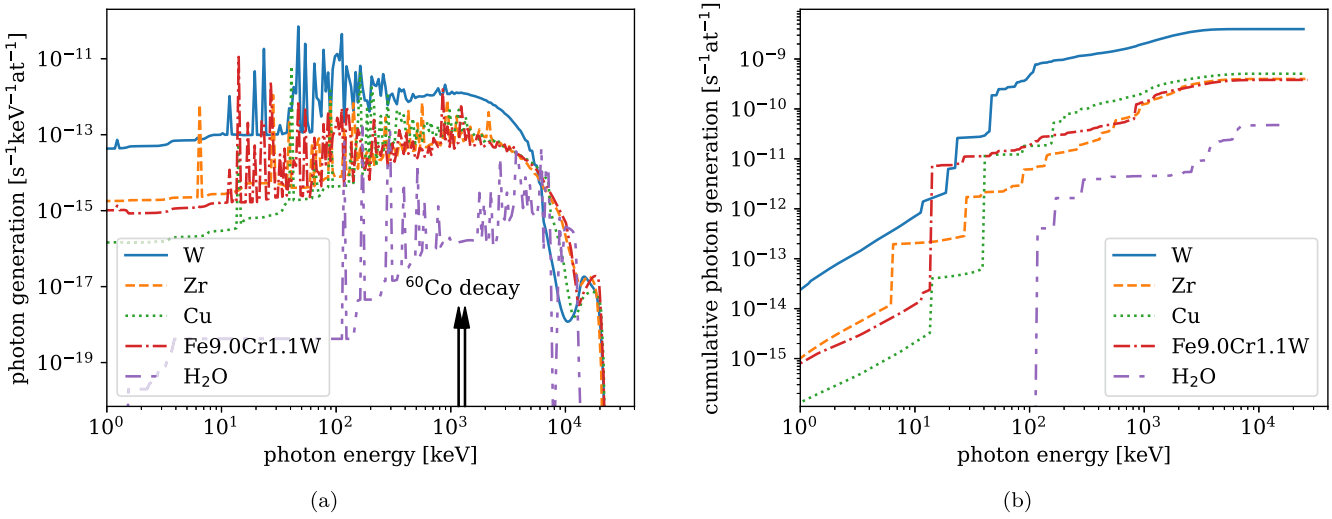

Fig. 3. (a) Photon generation in different materials induced by neutron irradiation corresponding to the DEMO spectrum in Fig. 2. The distributions are computed from the neutron spectra using the SPECTRA-PKA code with TENDL-2021 [4] nuclear data. The energies of the two 1.17 MeV and 1.33 MeV γ-photons emitted during the decay of ^{60}Co are indicated for comparison. (b) Cumulative photon generation obtained from (a), i.e. number of photons per unit time per atom that are generated with all energies up to the photon energy in the abscissa.

Table 2
Total photon generation in various materials obtained by integrating the energy-resolved spectra. The median generated photon energy is indicated although the distribution is highly non-symmetrical. The atomic density that was used to convert the per-atom quantities of SPECTRA-PKA is indicated in the last column.

Material	total generation [10^{13} s^{-1} cm^{-3}]	median energy [MeV]	atomic density [10^{22} at/cm^3]
W	25.1	1.02	6.31
Zr	1.71	1.78	4.30
Cu	4.12	1.23	8.12
Fe	2.94	1.35	8.50
Fe9.0Cr1.1W	3.24	1.35	8.50
H_2O	0.16	5.62	3.34

grid E_i, we define the energy differential photon generation term as $Q_{\mathrm{ph}}(E) = \sum_{i=1}^{N} Q_{\mathrm{ph}}^{(i)} \delta(E_{\mathrm{ph}} - E_i)$.

By integrating the photon generation spectra of Fig. 3 over the entire energy range, we obtain the total photon generation, and integrating up to half of this value we find a median photon generation energy for each of the five materials, plus Fe which was omitted from the figure for clarity as being very similar to Fe9.0Cr1.1W. All the values are reported in Table 2.

3.2. Photon and electron spectra for the fusion-relevant scenarios

Similarly to what we did for calculating the neutron-induced heating, we compare first the energy spectra of photons and electrons induced in various materials by the DEMO first wall neutron spectrum. The spectra are plotted in Fig. 4. The photon spectra were calculated taking the photon generation distributions of Fig. 3a as input for Eq. (9), with the resulting photon spectra acting as input for calculating the electron spectra following Eq. (14).

We quantified the effect of different neutron spectra, namely DEMO first wall, fission (HFR) and IFMIF, on the same materials, taking W and Fe9.0Cr1.1W as examples. The photon fluxes are shown in Fig. 5a and Fig. 5b, while the electron fluxes are shown in Fig. 5c and Fig. 5d, for Fe9.0Cr1.1W and W, respectively.

Different locations in future fusion reactors will experience different neutron fluxes. At the same time, different materials will be predominantly featured in the various components. To consider these two features, we extracted from a full neutronics calculation the neutron spectra expected in DEMO in the first wall, divertor, breeding blanket and vacuum vessel regions. We then used them as sources for the internal generation of photons and, in turn, electrons. The materials that were associated to the specific spectra were: W for the first wall, W and Cu for the divertor (i.e. taking in isolation the main components of the divertor "monoblock" being conceived for ITER and DEMO), Fe9.0Cr1.1W for the breeding blanket (where RAFM steels will be used) as a model alloy for Eurofer-97, and Fe18.0Cr10.0Ni for the vacuum vessel as a model alloy with chemical composition similar to austenitic stainless steel.

Fig. 6 shows the input neutron spectra and the calculated photon and electron spectra in this simplified scenario. The neutron spectra were obtained from an MCNP [28] simulation of a EU demonstration power plant (DEMO) with a helium-cooled bebble-bed blanket, see [17, 37] for details. The DEMO spectrum already introduced in Fig. 2 is the statistical tally scored in the outboard equatorial first wall of the design, built up from 10^9 source neutron trajectories. Alongside this spectrum in Fig. 6 are the spectra for three other regions of the reactor recorded in the same simulation: for the tritium breeding blanket behind the first wall (average spectrum across the ~1 m thickness of the breeding zone); for the high heat-flux armour of the divertor, which is the region where the exhaust gasses impinge on materials (as well has having a high neutron flux); and the primary containment vacuum vessel surrounding the blankets, divertor and plasma.

In Figs. 2, 5, and 6 we show several neutron, photon, and electron energy-differential spectra where the neutron distributions are used as input for calculating photon and electron distributions. By integration over energy or, as in our discrete case, by multiplication by bin width and summation, we can obtain the fluxes between given energy in-

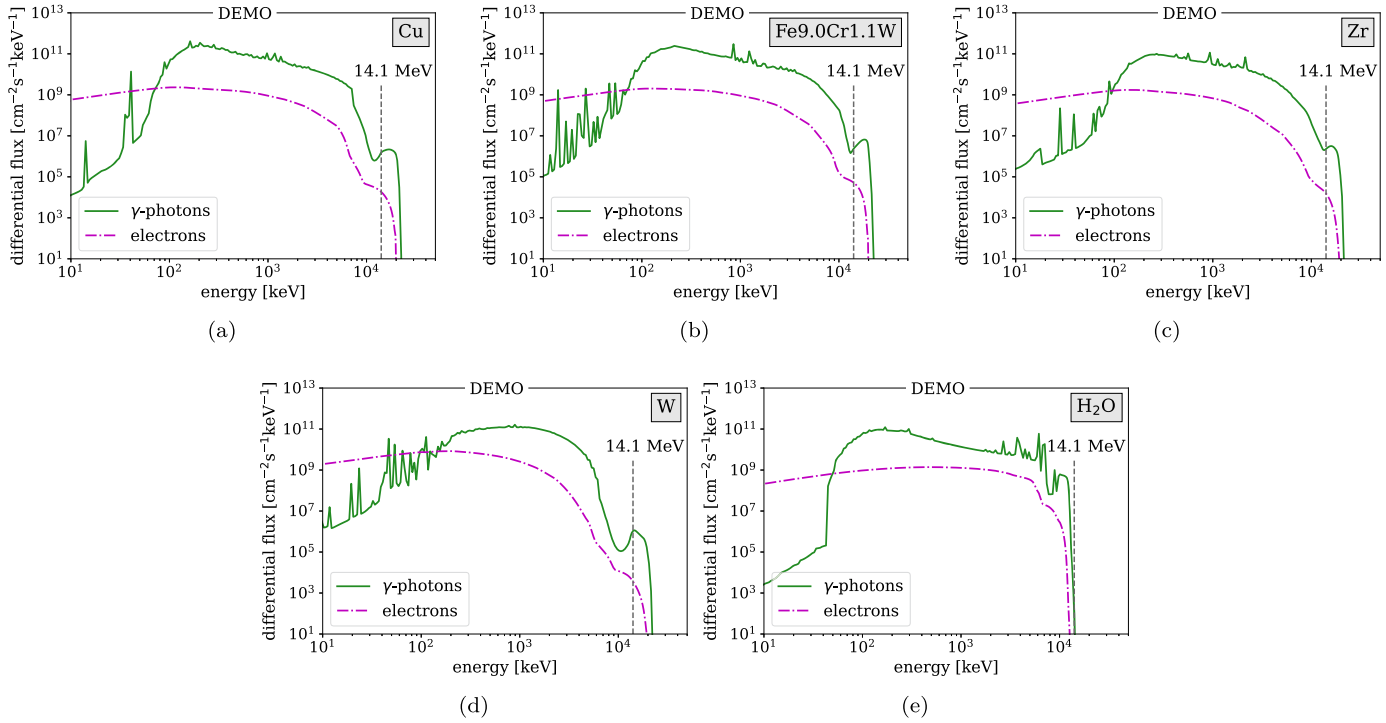

Fig. 4. Spectra of γ-photons and high-energy electrons in different materials under the neutron spectrum as seen by the DEMO first wall. The photon spectra follow from Fig. 3a, the electron spectra follow from the photon spectra shown here. All spectra, except those of water, extend beyond the 14.1 MeV line that marks the maximum neutron energy, indicating that some of the internal energy of the target nuclides is transferred to the generated γ-photons in the nonelastic reactions.

Table 3
Given neutron and calculated photon and electron fluxes for the materials and the locations in the DEMO reactor or in HFR or in IFMIF that were considered. The values, in units of $cm^{-2}\,s^{-1}$, were obtained by integrating the differential fluxes over energy E in the intervals indicated. In the first part of the table the data refer to the fluxes of Fig. 6 (FW: first wall, DIV: divertor, BB: breeding blanket, VV: vacuum vessel), in the second part of the table they refer to those in Figs. 2 and 5.

	Material	location	1 keV < E < 100 keV	100 keV < E < 1 MeV	E > 1 MeV	total
Φ_n		DEMO-FW	1.50×10^{14}	1.61×10^{14}	1.52×10^{14}	4.63×10^{14}
Φ_n		DEMO-DIV	1.34×10^{14}	1.63×10^{14}	1.09×10^{14}	4.07×10^{14}
Φ_n		DEMO-BB	5.87×10^{13}	3.89×10^{13}	3.04×10^{13}	1.28×10^{14}
Φ_n		DEMO-VV	8.03×10^{10}	5.12×10^{10}	2.50×10^{9}	1.34×10^{11}
Φ_{ph}	W	DEMO-FW	2.53×10^{11}	8.58×10^{13}	1.73×10^{14}	2.59×10^{14}
Φ_{ph}	W	DEMO-DIV	1.41×10^{11}	4.39×10^{13}	8.50×10^{13}	1.29×10^{14}
Φ_{ph}	Cu	DEMO-DIV	3.55×10^{11}	9.20×10^{13}	8.61×10^{13}	1.78×10^{14}
Φ_{ph}	Fe9.0Cr1.1W	DEMO-BB	1.23×10^{11}	2.56×10^{13}	2.31×10^{13}	4.88×10^{13}
Φ_{ph}	Fe18.0Cr10.0Ni	DEMO-VV	2.08×10^{8}	3.74×10^{10}	4.25×10^{10}	8.01×10^{10}
Φ_{el}	W	DEMO-FW	4.67×10^{11}	4.53×10^{12}	1.60×10^{12}	6.59×10^{12}
Φ_{el}	W	DEMO-DIV	2.41×10^{11}	2.27×10^{12}	7.80×10^{11}	3.29×10^{12}
Φ_{el}	Cu	DEMO-DIV	1.28×10^{11}	1.24×10^{12}	9.61×10^{11}	2.32×10^{12}
Φ_{el}	Fe9.0Cr1.1W	DEMO-BB	3.26×10^{10}	3.29×10^{11}	2.63×10^{11}	6.25×10^{11}
Φ_{el}	Fe18.0Cr10.0Ni	DEMO-VV	4.92×10^{7}	5.61×10^{8}	6.15×10^{8}	1.23×10^{9}
Φ_n		DEMO-FW	1.50×10^{14}	1.61×10^{14}	1.52×10^{14}	4.63×10^{14}
Φ_n		HFR	1.41×10^{14}	2.00×10^{14}	1.53×10^{14}	4.94×10^{14}
Φ_n		IFMIF	1.40×10^{13}	1.80×10^{14}	5.18×10^{14}	7.12×10^{14}
Φ_{ph}	W	DEMO-FW	2.53×10^{11}	8.58×10^{13}	1.73×10^{14}	2.59×10^{14}
Φ_{ph}	W	HFR	1.11×10^{12}	3.44×10^{14}	7.41×10^{14}	1.09×10^{15}
Φ_{ph}	W	IFMIF	2.41×10^{11}	6.50×10^{13}	9.80×10^{13}	1.63×10^{14}
Φ_{ph}	Fe9.0Cr1.1W	DEMO-FW	4.25×10^{11}	1.04×10^{14}	9.16×10^{13}	1.96×10^{14}
Φ_{ph}	Fe9.0Cr1.1W	HFR	9.54×10^{11}	1.38×10^{14}	1.48×10^{14}	2.86×10^{14}
Φ_{ph}	Fe9.0Cr1.1W	IFMIF	8.67×10^{11}	2.38×10^{14}	1.94×10^{14}	4.33×10^{14}
Φ_{el}	W	DEMO-FW	4.67×10^{11}	4.53×10^{12}	1.60×10^{12}	6.59×10^{12}
Φ_{el}	W	HFR	1.84×10^{12}	1.89×10^{13}	6.88×10^{12}	2.76×10^{13}
Φ_{el}	W	IFMIF	3.99×10^{11}	2.94×10^{12}	8.80×10^{11}	4.21×10^{12}
Φ_{el}	Fe9.0Cr1.1W	DEMO-FW	1.31×10^{11}	1.31×10^{12}	1.09×10^{12}	2.53×10^{12}
Φ_{el}	Fe9.0Cr1.1W	HFR	1.92×10^{11}	2.01×10^{12}	1.89×10^{12}	4.09×10^{12}
Φ_{el}	Fe9.0Cr1.1W	IFMIF	2.90×10^{11}	2.84×10^{12}	2.15×10^{12}	5.28×10^{12}

tervals. Table 3 provides the flux of particles with energy between 1 and 100 keV, between 100 keV and 1 MeV, and above 1 MeV. There are some general trends that can be observed. The neutron fluxes are approximately equipartitioned among the three intervals. Exceptions

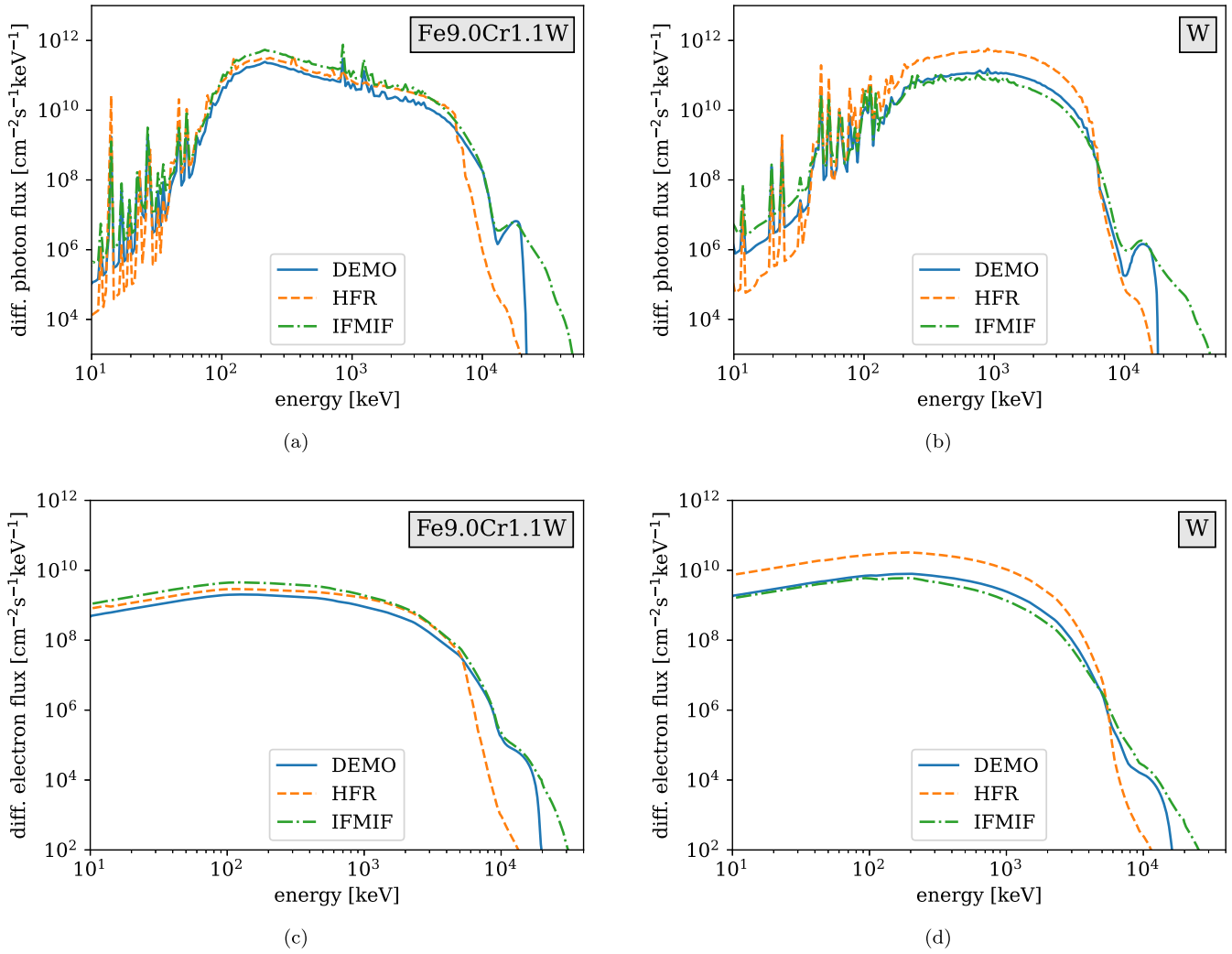

Fig. 5. Spectra of γ-photons (a, b) and high-energy electrons (c, d) for Fe9.0Cr1.1W (a, c) and W (b, d) under DEMO fusion scenario, the HFR fission scenario and the IFMIF neutron irradiation facility. Photon generation distributions were computed from the neutron spectra using the SPECTRA-PKA code with TENDL-2021 [4] nuclear data; the differential photon and electron distributions shown were then calculated with Eqs. (9) and (14).

are the vacuum vessel case, where lower energy neutrons are more abundant, and IFMIF, where higher energy neutrons are more numerous. The photon fluxes are approximately equipartitioned between the two higher-energy intervals, with comparatively fewer photons having lower energy. Electrons, on the other hand, are slightly more commonly found in the intermediate interval than in the higher. The total photon fluxes tend to be only slightly less intense than the total neutron fluxes, whereas electron fluxes at these high energies are between one and two orders of magnitude less intense. It should also be noted that the first interval is approximately one order of magnitude smaller than the second, which in turn is approximately one order of magnitude smaller than the third.

These results should be considered in light of the important assumption that only internal generation is relevant, and that materials are considered in isolation. In the reality, photons generated in different materials and in different locations in the reactor are all contributing to a total flux that is the superposition of the individual contributions. Monte Carlo calculations can in principle very accurately reproduce this real scenario. However, while transporting neutrons through a geometry is routine even for complex reactor geometries with modern tools and computer hardware, additionally transporting the photons generated by those neutrons becomes computationally challenging and even more extremely so if the electrons generated by the travelling photons are also themselves transported. For example, in our previous work [12], we performed combined neutron, photon, and electron transport simulations in simplified cubic geometry of pure W, which was flooded with the neutrons predicted for a first wall DEMO location obtained from a neutron-only run on a fully-detailed reactor design (this is the spectrum shown in Fig. 2). The input DEMO neutron spectrum was sampled to generate 10^7 source neutrons for transport through this simple geometry, but this led to the creation of approximately 3×10^8 photons via direct production during neutron reactions but also, predominantly, from bremsstrahlung and fluorescence. The transport of these photons subsequently led to the creation of almost 9×10^9 electrons, with more than 7×10^{11} individual electron tracking events. This corresponds to more than 70,000 electron events per source neutron. The simplified geometry allowed the scale-up in computation required to include photons and electrons to be acceptable in that case, but a similar attempt for a detailed reactor design would quickly become unfeasible due to the increased geometry complexity requiring a higher number of neutron histories to adequately sample the layout.

4. Discussion

The generation of γ-photons and high-energy electrons has several consequences that we discuss here. First, Table 1 shows the striking fact that photon heating in W approaches 100% of the total energy deposition, whereas neutron atomic recoil heating accounts for nearly 100%

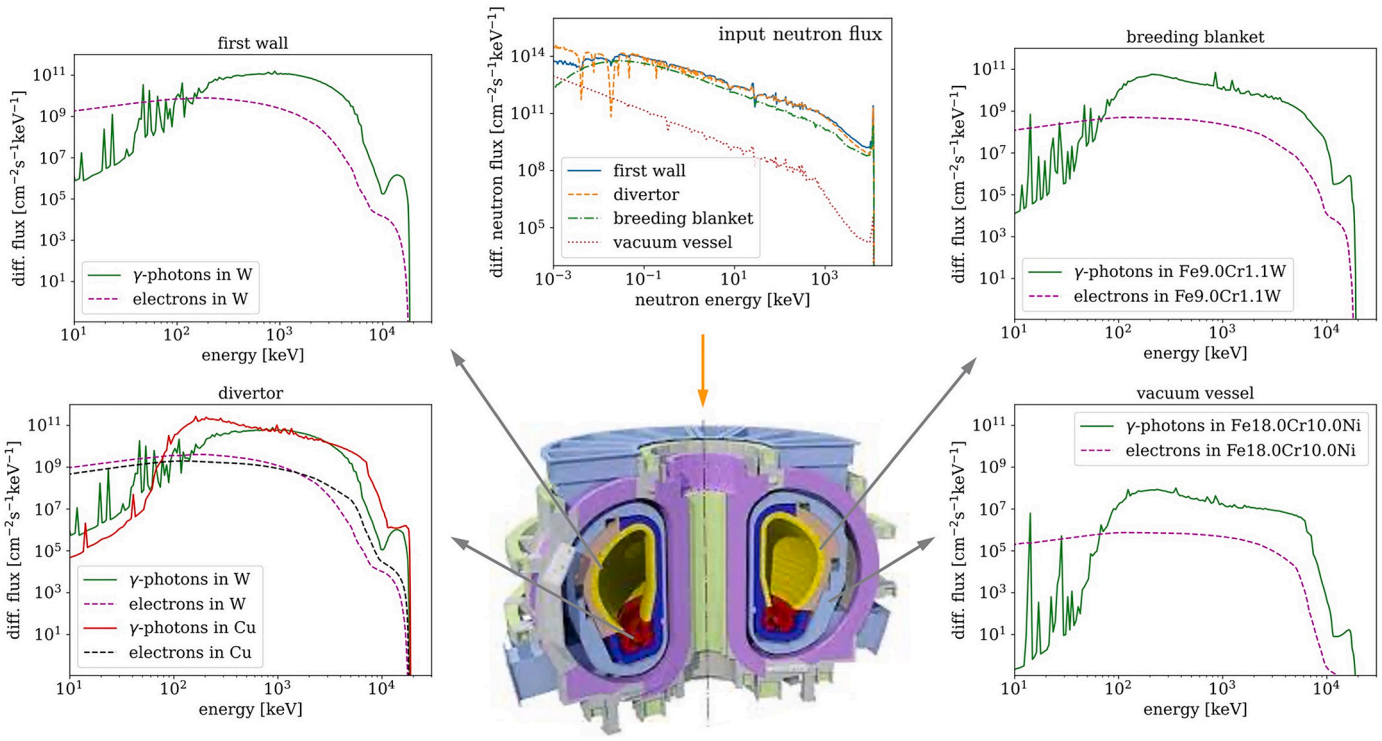

Fig. 6. Different regions of the reactor are exposed to different neutron fluxes (upper central panel). These generate photon and electron fluxes that are likewise position-dependent. The panels show the different photon and electron spectra that would be generated internally due to the different neutron fluxes. The mixing of radiation coming from other parts of the reactor—which is expected to be very important in the case of photons but less important for electrons—is not considered.

of the total energy deposition in Be. The two are the exact opposite of one another in this regard. This is interesting as both are candidate materials for the first wall; Be was originally used in JET before being replaced by W, and W is preferred for DEMO designs (ITER is being designed around Be, but the final selection is subject to change). The trend, however, is not linear with respect to nuclear mass. Already in Fe, in fact, photon heating accounts for 70 to 80% of the total heating in the two considered scenarios. The heating in all materials was found to be of the order of 1 to 10 W/g. It should be noted that this applies only to the energy deposited internally in the bulk of materials by *neutron irradiation*; there is an additional heat load on the surfaces of the tokamak chamber from exposure to fusion plasma.

As an example, the volumetric heating by the neutrons is not considered but it impacts the thermo-mechanical analysis of components such as the ITER divertor monoblock, where testing is carried out on the basis of pulses delivering a thermal load of 10 to 20 W/mm^2 [38] on the top surface of tiles having an area of 28×12 mm^2, for a total of about 3.4 to 6.7 kW. From Table 1 we can infer that there is an additional heat power that is not of convective origin of about 0.5 kW, considering the 30% of delayed heating as well. Photon heating remains substantially lower than convective heating, but it should nonetheless be incorporated in the analyses.

A second set of consequences involves the very high energy of the generated γ-radiation. Figs. 3 and 4 show that photons and electrons with energies up to about 20 MeV are to be expected in W, Zr, Cu, and Fe9.0Cr1.1W. This is considerably higher than the maximum neutron energy of 14.1 MeV, because the target nuclei decay to isotopes whose energy levels are lower than those of the original target nuclei. Some of the extra energy is released to the γ-photons generated by the decay process. From both Fig. 3 and Table 2 it is also clear that W, the heaviest of the considered targets, has the most intense γ-photon generation, whereas water, which conversely is the lightest, has the least intense generation. The difference is not as marked for the intermediate elements. Fe, Cu, and Zr have similar generation spectra (although with element-specific resonances) and cumulative photon generation. Such high-energy photons can enhance the corrosion of components exposed to water [39]; this is observed in carbon steel for instance [40]. Irradiation also enhances in-reactor corrosion of Zr-alloys, and one of the several mechanisms proposed to explain this is related to γ-induced production of radical species [41]. In the fusion scenario, corrosion is an important concern for CuCrZr alloys [42]. Looking at Fig. 6, we note that the CuCrZr pipes in the divertor region are exposed to the highest intensities of flux, comparable to the first wall region. Over the entire energy range considered, photon and electron fluxes for W in the divertor region are only smaller by a factor of about 2 with respect to the first wall. The decay of electronic excitations induced by the γ-photons is also detrimental to insulators [43,44].

Finally, there is also a problem specific to fusion posed by high-energy electrons, or "runaway electrons", as they foster instabilities in magnetised plasmas [45]. Runaway electrons are produced if electrons gain sufficient energy when electric fields are applied to the plasma, but there may also be a secondary cause given indirectly by neutron irradiation. In Appendix B we derive formulae for estimating both the total electron flux escaping the surface of a volume containing a source of high-energy electrons, and the mean energy of the escaped electrons. The total flux is

$$\Phi_{\mathrm{esc}} = \frac{1}{4} \sum_i Q_i R(E_i). \tag{24}$$

Note that here the elements of the volumetric source term Q_i, in cm^{-3} s^{-1}, are the electrons generated inside the i-th energy bin E_i. This is the discrete representation, defined in (B2), of the source term of the electron flux of Eq. (14), which has units of cm^{-3} s^{-1} eV^{-1}.

Electrons excited with initial energy E_i continuously lose energy while travelling the range $R(E_i)$ given by Eq. (13). They can escape the surface with an escape energy $0 < E_{\mathrm{esc}} < E_i$, depending on the distance from the surface. The distribution of E_{esc}, derived in Appendix B, is

$$P(E_{\mathrm{esc}}) = \frac{1}{R(E_i)\bar{\varepsilon}(E_{\mathrm{esc}})}, 0 < E_{\mathrm{esc}} < E_i. \tag{25}$$

Hence, the mean escape energy is

$$\overline{E}^{(i)}_{\mathrm{esc}} = \int_0^{E_i} E' P(E') \mathrm{d}E'. \tag{26}$$

Since the number of electrons excited with initial energy E_i is proportional to Q_i, we then define a weighed average of the mean energies using the Q_i values as weights,

$$\overline{E}_{\mathrm{esc}} = \frac{\sum_i Q_i \overline{E}^{(i)}_{\mathrm{esc}}}{\sum_i Q_i}. \tag{27}$$

Using the source term generating the DEMO electron flux in W of Fig. 4, the total flux escaping a surface is 1.8×10^{12} cm^{-2} s^{-1}, at an average energy of about 330 keV, which is well into the runaway range.

A third consequence of the photon and electron generation by neutrons is that it adds another dimension to the possible differences between irradiation environments, which is important in the context of experimental studies. The greatest difference is between ion and neutron irradiation, as in the former the neutron-stimulated γ-emission is not present. However, also different neutron sources—characterised by different energy spectra—produce unequal populations of photons and electrons. These differences depend on atomic and isotopic nature of the irradiated material. This is the reason for displaying the spectra in Fig. 5. Using these spectra, we can assess whether the IFMIF facility generates a neutron irradiation environment similar to that of a fusion power plant, at least as far as the excited γ-photons and high-energy electrons are concerned. In W, both photon and electron spectra in IFMIF follow quite closely those expected in DEMO, even around the 10 MeV energies. There is a noticeable flux above 20 MeV in IFMIF which should be absent in DEMO, but the intensity is small in comparison with the rest of the spectrum. In Fe9.0Cr1.1W, the photon and electron generation in IFMIF is slightly higher than in DEMO, but is still very similar. Our assessment focuses on a separate aspect of IFMIF than that considered by Simakov *et al.* [14], which was focused on the expected surviving defects under neutron irradiation in DEMO, HFR, and IFMIF, but they both suggest that IFMIF is expected to be an appropriate neutron source suitable for its intended purpose.

5. Conclusions

We investigated the generation of prompt γ-photons and high-energy electrons in fusion-relevant materials such as tungsten, the ferritic steel alloy Fe9.0Cr1.1W, and copper. The energy deposited by neutrons with typical fusion or fission energy spectra is primarily transformed into γ-radiation, with the conversion factor of about 70 to 99% in iron, copper, and tungsten. On the other hand, γ-heating is less intense in zirconium and almost nonexistent in beryllium. This agrees with previous studies [10–12]. In water, the γ-generation is less intense, but the spectra remain higher than in the aforementioned metals and alloys in the energy range approaching 10 MeV.

The spectra of photons and electrons generated by neutrons extend up to energies of about 20 MeV under the expected neutron flux at the location of plasma-facing components of DEMO, with the peak of the spectrum in the hundreds of keV range. The similar intensity of the neutron flux in the first wall and in the divertor regions results in similar production rates of γ-photons and electrons, while the generation in the breeding blanket is slightly lower.

Finally, we evaluated the photon and electron generation in W and in Fe9.0Cr1.1W and found the expected fluxes for the IFMIF material testing facility to be similar to those expected in DEMO and HFR reactors.

CRediT authorship contribution statement

Luca Reali: Formal analysis, Investigation, Methodology, Software, Validation, Visualization, Writing – original draft. **Mark R. Gilbert:** Data curation, Investigation, Methodology, Software, Writing – review & editing. **Max Boleininger:** Formal analysis, Methodology, Writing – review & editing. **Sergei L. Dudarev:** Conceptualization, Formal analysis, Methodology, Project administration, Writing – review & editing.

Declaration of competing interest

The authors declare the following financial interests/personal relationships which may be considered as potential competing interests:

L. Reali, M. Boleininger, S.L. Dudarev reports financial support was provided by European Consortium for the Development of Fusion Energy. L. Reali, M. Boleininger, S.L. Dudarev reports financial support was provided by UK Research and Innovation.

Data availability

The data and the scripts supporting this publication are available at: https://doi.org/10.14468/hyde-5x49.

Acknowledgements

The authors are grateful to M. Rieth, D. Terentyev, S. Kalcheva, G. Pintsuk, G. Aiello, D. R. Mason and P. Helander for stimulating discussions. This work has been carried out within the framework of the EUROfusion Consortium, funded by the European Union via the Euratom Research and Training Programme (Grant Agreement No 101052200 — EUROfusion) and was partially supported by the Broader Approach Phase II agreement under the PA of IFERC2-T2PA02. This work was also funded by the EPSRC Energy Programme (grant number EP/W006839/1). To obtain further information on the data and models underlying the paper please contact PublicationsManager@ukaea.uk. Views and opinions expressed are however those of the authors only and do not necessarily reflect those of the European Union or the European Commission. Neither the European Union nor the European Commission can be held responsible for them. We gratefully acknowledge the provision of computing resources by the IRIS (STFC) Consortium.

Appendix A. The energy dependence of the photon generation

The DEMO first wall spectrum (same as in Fig. 2) was divided into three parts according to the neutron energy: thermal neutrons with energy up to 0.25 eV, epithermal neutrons with energy higher than 0.25 eV and lower than 100 keV, and fast neutrons with energy above 100 keV, see Fig. 7a. This was done to understand if one of the three sections was responsible for the production of most of the photons, and the energy spectrum of the three fractions of the total. We then considered the three parts of the neutron flux as if isolated and calculated the three corresponding photon generation distributions per target atom in W and in Fe9.0Cr1.1W. The distributions are plotted in Figs. 7b and 7c, respectively, and compared with the total (which is the same as in Fig. 3a). Changing the cutoff between epithermal and fast neutrons from 100 keV to 1 MeV causes a negligible change in the results on both W and Fe9.0Cr1.1W.

The total photon generation was 3.972×10^{-9} photons per second per W atom and 3.815×10^{-10} photons per second per atom in Fe9.0Cr1.1W. Of these quantities, as specified also in Fig. 7a, only a negligible fraction was ascribed to the thermal part of the DEMO spectrum. Conversely, the epithermal section led to the generation of about 71% of the photons in W and 15% in Fe9.0Cr1.1W. The situation was reversed for the fast section of the DEMO spectrum, which produced the remaining 29% and 85% in the two materials, respectively. We therefore found another marked difference coming from the element-specific energy dependence of the nuclear cross sections. Another difference is visible from Figs. 7b and 7c. Fast neutrons dominate the photon generation throughout the entire energy spectrum in Fe9.0Cr1.1W. On the other hand, although epithermal neutrons produce the majority of photons in W, the photons

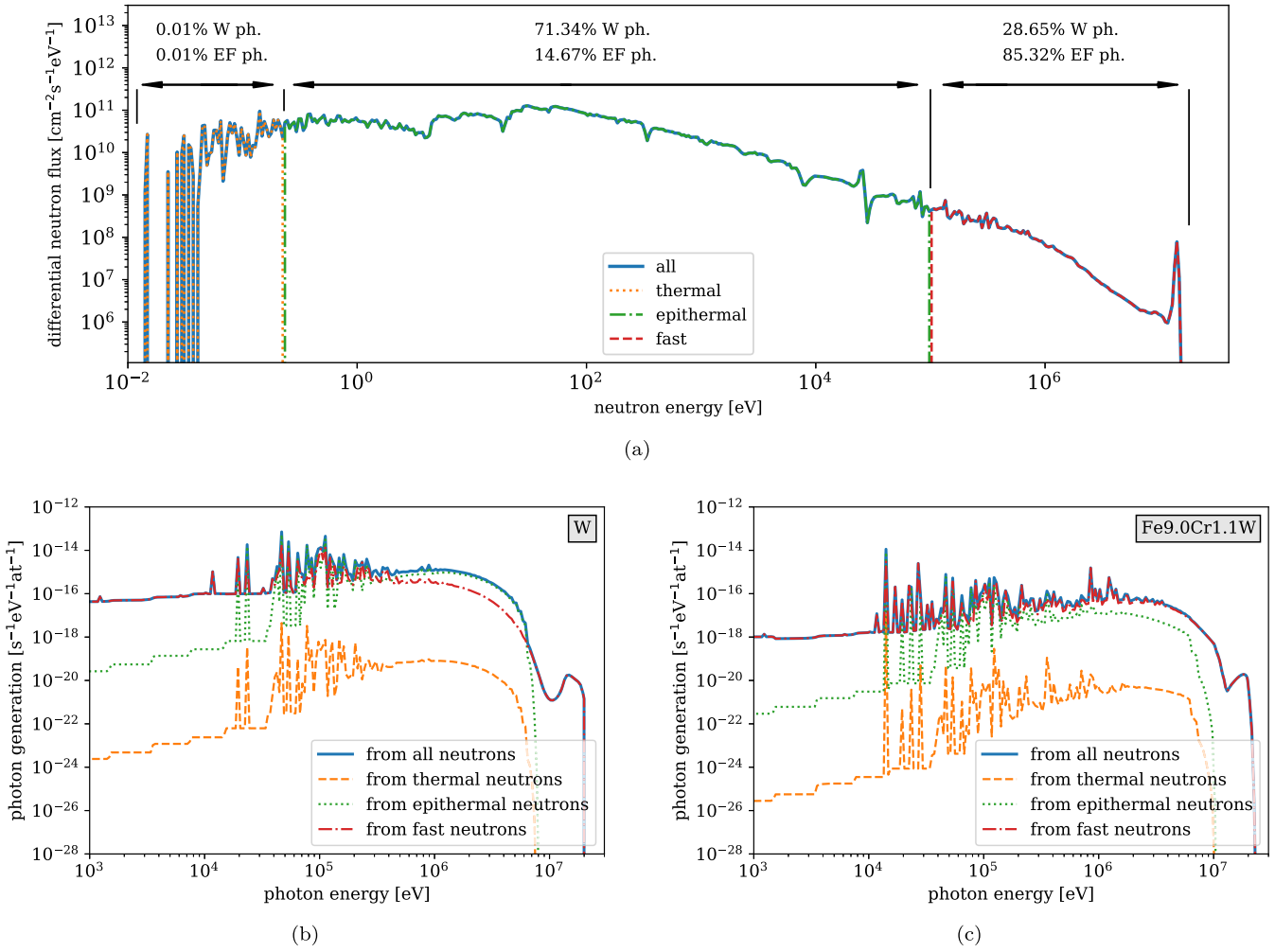

Fig. 7. (a) The DEMO first wall neutron spectrum was split into three parts: thermal neutrons with energy below 0.25 eV, epithermal neutrons with an intermediate energy between 0.25 eV and 100 keV, and fast neutrons with energy greater than 100 keV. The fractions of the total photon generation induced by the three portions of the spectrum are indicated for pure W and for Fe9.0Cr1.1W (EF in the figure, short for simplified Eurofer-97). The energy-resolved photon generation is shown in (b) for Fe9.0Cr1.1W and in (c) for W. Fast neutrons are responsible for the generation of most of the photons in Fe9.0Cr1.1W, as well as of the most and least energetic photons in W, where however the majority of photons are generated with energies of a few MeV because of collisions initiated by epithermal neutrons.

that are released with the lowest and highest energies originate from collisions with fast neutrons. It can also be noted that the epithermal generation, i.e. that caused by neutrons of energy up to 100 keV, peaks at about 1 MeV in W, implying that the majority of the photon energy was in this case released by the decaying nuclei.

Appendix B. Estimate of electrons emission from a surface

Some of the electrons excited by the γ flux near the surface of a tokamak wall have sufficient energy to escape and be emitted into the plasma. We provide here an estimate of the number of escaping electrons and their associated energy. This is only approximate as it assumes that electrons travel along straight paths.

High-energy electrons are excited at a rate given by the volumetric source term $Q_{\mathrm{el}}(E)$ that enters Eq. (12) and in a randomly oriented direction. We consider electrons excited near a flat surface and assume that they travel along straight paths continuously losing energy according to Eq. (13). For a given excitation energy, the maximum depth from which an electron can escape is its range $R(E)$. We call z the depth from the surface; θ is the angle between the starting direction and the direction normal to the surface; α is the azimuthal angle. The distance between the excitation point and the surface is $z/\cos\theta$. We then find all the electrons that contribute to the flux of escaping electrons Φ_{esc} by integrating $Q_{\mathrm{el}}(E)$ over all excitation energies E, depths z and directions; a Heaviside step function $\Theta()$ ensures that the electron can only escape if the distance from the surface is less than its range. This leads to the integral

$$\Phi_{\mathrm{esc}} = \int_0^{\infty} \mathrm{d}E \int_0^{R(E)} \mathrm{d}z \int_0^{2\pi} \mathrm{d}\alpha \int_0^{\pi/2} \mathrm{d}\theta \sin\theta \left[Q_{\mathrm{el}}(E)\Theta\left(R(E) - \frac{z}{\cos\theta}\right)\right]. \tag{B1}$$

We note that θ only runs up to $\frac{\pi}{2}$ excluding the electrons excited away from the surface. The source term is given as the discrete array

$$Q_{\mathrm{el}}(E) = \frac{1}{4\pi} \sum_i Q_i \delta(E - E_i). \tag{B2}$$

By changing the variable of the Heaviside step function to $t = R(E) - z/\cos\theta$, or otherwise, the integrals can be readily solved yielding the total flux, stated in Eq. (24),

$$\Phi_{\mathrm{esc}} = \frac{1}{4} \sum_i Q_i R(E_i). \tag{B3}$$

To estimate the energy of the escaping electrons, we find the probability distribution $P(E_{\mathrm{esc}})$ of an electron escaping with energy E_{esc}. We begin modelling the excitation of the electron with energy E as a pro-

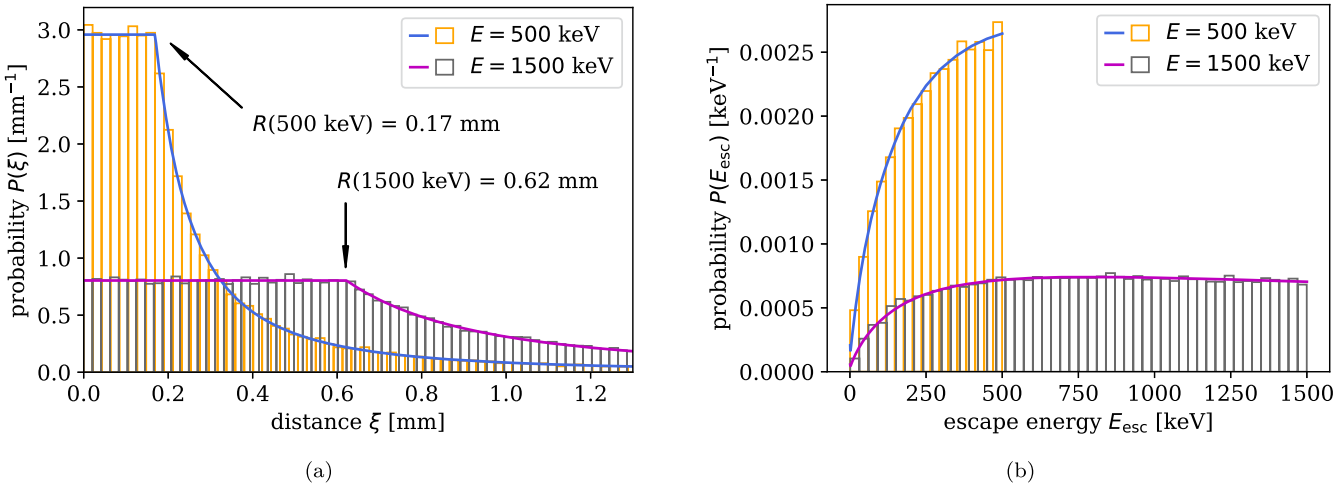

Fig. 8. Numerical test simulating 100,000 electrons excited in a random direction and at a random depth within the range $R(E)$ for the energies of 500 and 1500 keV. (a) Distribution of distance travelled before hitting the surface, noting that the distance by which the electron loses all of its energy is where the distribution is no longer uniform. (b) Distribution of energy after escaping the surface of the electrons that hit the surface before losing all of their energy. Eq (B6) and Eq. (B11) show very good agreement with the numerical test. (For interpretation of the colours in the figure(s), the reader is referred to the web version of this article.)

cess characterised by randomly distributed depth z and direction angle θ defined above. z is uniformly distributed over $[0, R(E)]$. θ obeys the distribution $P(\theta) = \sin\theta$ over $[0, \pi/2]$. We then calculate the distribution of the distance to the surface $\xi = z/\cos\theta$.

First, we show that the distribution $P(y)$ of $y = \cos\theta$ is

$$P(y) = \int_{-\infty}^{\infty} \sin\theta\,\delta(y - \cos\theta)\mathrm{d}\theta = \int_{y-1}^{y} \delta(t)\mathrm{d}t$$

$$= \begin{cases} 1, & 0 < y < 1 \\ 0, & \text{otherwise.} \end{cases} \tag{B4}$$

That is, ξ is the ratio of two uniformly distributed numbers. Using the ratio distribution of independent variables we write

$$P(\xi) = \int_{-\infty}^{\infty} \left[\frac{\Theta(\xi y) - \Theta(\xi y - R(E))}{R(E)}\right]\left[\frac{\Theta(y) - \Theta(1-y)}{1}\right]\mathrm{d}y$$

$$= \int_{0}^{1} \frac{\Theta(\xi y) - \Theta(\xi y - R(E))}{R(E)}\mathrm{d}y, \tag{B5}$$

which evaluates to

$$P(\xi) = \begin{cases} \frac{1}{2R(E)}, & 0 < \xi < R(E) \\ \frac{R(E)}{2\xi^2}, & \xi > R(E). \end{cases} \tag{B6}$$

Noting that the electrons that escape are those whose distance $\xi \le R(E)$, we see that in this region also $P(\xi)$ has a uniform distribution. Next, we point out the relation between the distance ξ and the escape energy E_{esc}:

$$\xi = \int_{E_{\mathrm{esc}}}^{E} \frac{\mathrm{d}E'}{\overline{\varepsilon}(E')}. \tag{B7}$$

The target distribution $P(E_{\mathrm{esc}})$ follows from the distribution of ξ by a change of variable as

$$P(E_{\mathrm{esc}}) = P\big(\xi(E_{\mathrm{esc}})\big)\left|\frac{\mathrm{d}\xi}{\mathrm{d}E_{\mathrm{esc}}}\right|. \tag{B8}$$

Equivalently, Eq. (B7) can be written as

$$R(E) - \xi = \int_{0}^{E_{\mathrm{esc}}} \frac{\mathrm{d}E'}{\overline{\varepsilon}(E')}, \tag{B9}$$

from which it follows that

$$-\frac{\mathrm{d}\xi}{\mathrm{d}E_{\mathrm{esc}}} = \frac{1}{\overline{\varepsilon}(E_{\mathrm{esc}})}. \tag{B10}$$

Hence, the distribution of escape energies—stated in Eq. (25)—is

$$P(E_{\mathrm{esc}}) = \frac{1}{R(E)\overline{\varepsilon}(E_{\mathrm{esc}})}, 0 < E_{\mathrm{esc}} < E. \tag{B11}$$

From this we calculate the mean energy, or the first moment of the distribution

$$\overline{E}_{\mathrm{esc}} = \int_{0}^{E} E' P(E')\mathrm{d}E'. \tag{B12}$$

Fig. 8 shows the numerical comparison of a random sample of 100,000 elements and the probability distributions of ξ and E_{esc}, (B6) and (B11).

For the fusion-relevant case of a spectrum of electron source terms, Eq. (B2), each element in the array corresponds to an excitation energy and therefore to a distribution of escape energies. We calculate a weighted average of the mean escape energies by taking the Q_i as the weights, which is stated in Eq. (27).

References

[1] F. Wagner, Physics of Magnetic Confinement Fusion, EPJ Web of Conferences, vol. 54, EDP Sciences, 2013, p. 01007.
[2] H.T. Motz, Neutron capture gamma-ray spectroscopy, Annu. Rev. Nucl. Sci. 20 (1970) 1.
[3] A. Barzilov, I. Novikov, Material classification by analysis of prompt photon spectra induced by 14-MeV neutrons, Phys. Proc. 66 (2015) 396.
[4] A.J. Koning, D. Rochman, J.-Ch. Sublet, TENDL-2021, https://tendl.web.psi.ch/tendl_2021/tendl2021.html, 2021. (Accessed 30 December 2021).
[5] I.L. Morgan, Inelastic scattering of neutrons, Phys. Rev. 103 (1956) 1031.
[6] Y. Wu, Fusion Neutronics, Springer, 2017.
[7] G. Molnár, R.M. Lindstrom, Nuclear reaction prompt gamma-ray analysis, Nucl. Methods Mineral. Geol. Tech. Appl. (1998) 145.
[8] S. Hlaváč, P. Obložinskỳ, Nanosecond timing in prompt γ ray analysis of bulk media using fast neutrons, Nucl. Instrum. Methods Phys. Res., Sect. B, Beam Interact. Mater. Atoms 28 (1987) 93.
[9] S.A. Johansson, Gamma de-excitation of fission fragments: (II). Delayed radiation, Nucl. Phys. 64 (1965) 147.

[10] M. Abdou, C. Maynard, Calculational methods for nuclear heating—part II: applications to fusion-reactor blankets and shields, Nucl. Sci. Eng. 56 (1975) 381.
[11] K. Ambrožič, A. Gruel, V. Radulović, M. Le Guillou, P. Blaise, C. Destouches, L. Snoj, Delayed gamma determination at the JSI TRIGA reactor by synchronous measurements with fission and ionization chambers, Nucl. Instrum. Methods Phys. Res., Sect. A, Accel. Spectrom. Detect. Assoc. Equip. 911 (2018) 94.
[12] L. Reali, M.R. Gilbert, M. Boleininger, S.L. Dudarev, Intense γ-photon and high-energy electron production by neutron irradiation: effects of nuclear excitations on reactor materials, PRX Energy 2 (2023) 023008.
[13] G. Rimpault, D. Bernard, D. Blanchet, C. Vaglio-Gaudard, S. Ravaux, A. Santamarina, Needs of accurate prompt and delayed γ-spectrum and multiplicity for nuclear reactor designs, Phys. Proc. 31 (2012) 3.
[14] S. Simakov, A.Y. Konobeyev, U. Fischer, V. Heinzel, Comparative study of survived displacement damage defects in iron irradiated in IFMIF and fusion power reactors, J. Nucl. Mater. 386 (2009) 52.
[15] W. Królas, A. Ibarra, The IFMIF-DONES project, Nucl. Phys. News 29 (2019) 28.
[16] J. Knaster, P. Garin, H. Matsumoto, Y. Okumura, M. Sugimoto, F. Arbeiter, P. Cara, S. Chel, A. Facco, P. Favuzza, T. Furukawa, R. Heidinger, A. Ibarra, T. Kanemura, A. Kasugai, H. Kondo, V. Massaut, J. Molla, G. Micciche, S. O'hira, K. Sakamoto, T. Yokomine, E. Wakai, IFMIF/EVEDA Integrated Project Team, Overview of the IFMIF/EVEDA projecta, Nucl. Fusion 57 (2017) 102016.
[17] M. Gilbert, T. Eade, C. Bachmann, U. Fischer, N. Taylor, Activation, decay heat, and waste classification studies of the European DEMO concept, Nucl. Fusion 57 (2017) 046015.
[18] M.J. Lloyd, A.J. London, J. Haley, M.R. Gilbert, C.S. Becquart, C. Domain, E. Martinez, M.P. Moody, P.A.J. Bagot, D. Nguyen-Manh, D.E.J. Armstrong, Interaction of transmutation products with precipitates, dislocations and grain boundaries in neutron irradiated W, Materialia 22 (2022) 101370.
[19] M.H.H. Kolb, M. Bruns, R. Knitter, S. van Til, Lithium orthosilicate surfaces: characterization and effect on tritium release, J. Nucl. Mater. 427 (2012) 126.
[20] S.J. Zinkle, A. Möslang, Evaluation of irradiation facility options for fusion materials research and development, Fusion Eng. Des. 88 (2013) 472, in: Proceedings of the 27th Symposium on Fusion Technology (SOFT-27), Liège, Belgium, September 24-28, 2012.
[21] O.N. Vassiliev, Monte Carlo Methods for Radiation Transport, Springer, 2017.
[22] M.J. Berger, J.H. Hubbell, XCOM: Photon cross sections on a personal computer, Tech. Rep., Bureau of Standards, Center for Radiation Research, Washington, DC, USA, 1987.
[23] M.R. Gilbert, J. Marian, J.-C. Sublet, Energy spectra of primary knock-on atoms under neutron irradiation, J. Nucl. Mater. 467 (2015) 121.
[24] R. MacFarlane, D.W. Muir, R. Boicourt, A.C. Kahler III, J.L. Conlin, The NJOY nuclear data processing system, version 2016, Tech. Rep., Los Alamos National Lab. (LANL), Los Alamos, NM, United States, 2017.
[25] H. Niedrig, Electron backscattering from thin films, J. Appl. Phys. 53 (1982) R15.
[26] S.L. Dudarev, P. Rez, M.J. Whelan, Theory of electron backscattering from crystals, Phys. Rev. B 51 (1995) 3397.
[27] F.B. Brown, R.F. Barrett, T.E. Booth, J.S. Bull, L.J. Cox, R.A. Forster, T.J. Goorley, R.D. Mosteller, S.E. Post, R.E. Prael, E.C. Selcow, A. Sood, J. Sweezy, MCNP version 5, Trans. Am. Nucl. Soc. 87 (2002) 273.
[28] C.J. Werner, et al., MCNP Users Manual - Code Version 6.2, Tech. Rep. report LA-UR-17-29981, Los Alamos National Laboratory, 2017, further details at http://mcnp.lanl.gov/.
[29] N.P. Kalashnikov, V.S. Remizovich, M.I. Ryazanov, Collisions of Fast Charged Particles in Solids, Gordon and Breach Science Publishers Inc., New York, 1985.
[30] M.J. Berger, J.S. Coursey, M.A. Zucker, et al., ESTAR, PSTAR, and ASTAR: computer programs for calculating stopping-power and range tables for electrons, protons, and helium ions (version 1.21), Tech. Rep., National Institute of Standards and Technology, Gaithersburg, MD, 1999.
[31] H. Bethe, Bremsformel für elektronen relativistischer geschwindigkeit, Z. Phys. 76 (1932) 293–299.
[32] R. Fitzgerald, K. Keil, K.F.J. Heinrich, Solid-state energy-dispersion spectrometer for electron-microprobe X-ray analysis, Science 159 (1968) 528.
[33] L. Reimer, Transmission Electron Microscopy, 2nd ed., Springer, 1989.
[34] J.-Ch. Sublet, J.W. Eastwood, J.G. Morgan, M.R. Gilbert, M. Fleming, W. Arter, FISPACT-II: an advanced simulation system for activation, transmutation and material modelling, Nucl. Data Sheets 139 (2017) 77.
[35] E. Lucon, R. Chaouadi, M. Decréton, Mechanical properties of the European reference RAFM steel (EUROFER97) before and after irradiation at 300 C, J. Nucl. Mater. 329 (2004) 1078.
[36] R. Klueh, Elevated temperature ferritic and martensitic steels and their application to future nuclear reactors, Int. Mater. Rev. 50 (2005) 287.
[37] M.R. Gilbert, J.-Ch. Sublet, Handbook of activation, transmutation, and radiation damage properties of the elements simulated using FISPACT-II & TENDL-2015, Magnetic Fusion Plants, Tech. Rep. CCFE-R(16)36 (UKAEA, 2016) available from, http://fispact.ukaea.uk.
[38] M. Fursdon, J.-H. You, M. Li, Towards reliable design-by-analysis for divertor plasma facing components–guidelines for inelastic assessment (part 1: unirradiated), Fusion Eng. Des. 147 (2019) 111234.
[39] P. Wang, S. Grdanovska, D.M. Bartels, G.S. Was, Effect of radiation damage and water radiolysis on corrosion of FeCrAl alloys in hydrogenated water, J. Nucl. Mater. 533 (2020) 152108.
[40] K. Daub, X. Zhang, J. Noel, J. Wren, Gamma-radiation-induced corrosion of carbon steel in neutral and mildly basic water at 150 °C, Corros. Sci. 53 (2011) 11.
[41] B. Cox, Some thoughts on the mechanisms of in-reactor corrosion of zirconium alloys, J. Nucl. Mater. 336 (2005) 331.
[42] C. Obitz, J. Öijerholm, S. Wikman, E. Bratu, Erosion corrosion of CuCrZr specimens exposed for simulated ITER operational conditions, Nucl. Mater. Energy 9 (2016) 261.
[43] C.B. Lushchik, A.C. Lushchik, Decay of Electronic Excitations with Formation of Defects in Solids, Nauka, Moscow, USSR, 1989.
[44] C.B. Lushchik, I.K. Vitol, M.A. Elango, Decay of electronic excitations into radiation defects in ionic crystals, Sov. Phys. Usp. 20 (1977) 489.
[45] B.N. Breizman, P. Aleynikov, E.M. Hollmann, M. Lehnen, Physics of runaway electrons in tokamaks, Nucl. Fusion 59 (2019) 083001.